Supporting Information

Significantly (00*l*)-textured Ag_2Se thin films with excellent thermoelectric performance for flexible power applications

Zhuang-Hao Zheng,[a] Yi-Liu Li,[a] Jun-Yu Niu,[a] Meng Wei,[a,] Dong-Liang Zhang,[a] Yi-Ming Zhong,[a] Mohammad Nisar,[a] Adeel Abbas,[a] Shuo Chen,[a] Fu Li,[a] Guang-Xing Liang,[a] Ping Fan,[a] Yue-Xing Chen,[a] **

[a] Shenzhen Key Laboratory of Advanced Thin Films and Applications, Key Laboratory of Optoelectronic Devices and Systems of Ministry of Education and Guangdong Province, College of Physics and Optoelectronic Engineering, Shenzhen University, Shenzhen 518060, P. R. China.

* Corresponding author, Email: mengwei@szu.edu.cn and chenyx@szu.edu.cn

Table S1 Composition content and thickness of the thin films deposited at different temperature

Deposition temperature (K)	303	333	363	393	423	453	483
Se (at%)	32.7	32.8	32.8	32.7	32.7	32.6	32.5
Ag (at%)	67.3	67.2	67.2	67.3	67.3	67.4	67.5
Actual atomic ratio (Ag/Se)	2.06	2.05	2.05	2.06	2.06	2.07	2.08
Thickness (nm)	463	455	458	470	455	450	448

Table S2 Composition content and thickness of the thin films with different Ag and Se content

Nominal atomic ratio (Ag/Se)	1.94	1.96	1.98	2.00	2.02	2.04
Se (at%)	33.33	33.16	32.94	32.71	32.46	32.23
Ag (at%)	66.67	66.84	67.06	67.29	67.54	67.77
Actual atomic ratio (Ag/Se)	2.00	2.02	2.04	2.06	2.08	2.10
Thickness (nm)	455	450	460	457	450	455

Table S3 Room-temperature thermoelectric performance of *p*-type Sb_2Te_3 thin films.

Material	σ (S cm^{-1})	S (μV K^{-1})	$S^2\sigma$ (μW cm^{-1} K^{-1})
Sb_2Te_3	513.6	143.2	10.5

P-type Sb_2Te_3 thin films were deposited on the flexible polyimide (PI) substrate by thermal evaporation method. The deposition power of the evaporation source for Sb_2Te_3 powder was ~ 90 W under a background vacuum pressure of 3.0×10^{-3} Pa. The deposition time of Sb_2Te_3 was 15 mins with the thickness about 650 nm.

Table S4. Comparison of output power density ω_{out} of the flexible devices among others

reports**.** Here PVP is abbreviated from polyvinylpyrrolidone, PPy is abbreviated from polypyrrole, NWs are abbreviated from nanowires, PEDOT:PSS is abbreviated from poly(3,4-ethylenedioxythiophene):poly(styrene sulfonate), PANI is abbreviated from polyaniline, and SWCNT is abbreviated from single-wall carbon nanotube.

p-type Material	*n*-type Material	Substrate	Unit	ΔT (K)	ω_{out} (mW cm^{-2})	Ref.
Sb_2Te_3	Ag_2Se	polyimide	8	50	~3.71	This work
-	Ag_2Se/Ag/Cu AgSe	nylon membrane	6	45	~0.542	[1]
-	PVP/Ag_2Se	polyimide	6	29.1	~2.88	[2]
-	Ag_2Se/Se/PPy	nylon membrane	6	34.1	~3.76	[3]
Cu_2Se NWs + PEDOT:PSS	-	polyimide	9	30	0.091	[4]
PANI/SWCNT/Te	-	-	4	40	0.0624	[5]
$Bi_{0.5}Sb_{1.5}Te_3$	Bi_2Te_3	polyimide	3	40	0.8978	[6]

The power density (P_D) is calculated by $P_D = \frac{P_{max}}{N \cdot A} = \frac{P_{max}}{N \cdot T \cdot w}$,[4] where N, A, and l denotes the number, the length and the area of the legs, T, w denote the thickness (450 nm for Ag_2Se film, and 650 nm for Sb_2Te_3 film) and the width (2.5 mm).

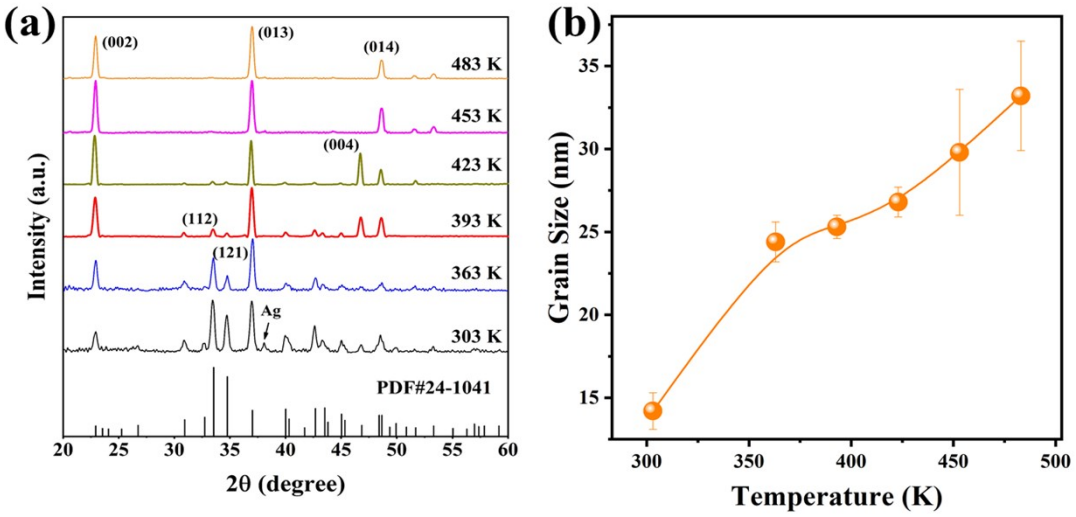

Fig. S1 (a) XRD patterns of thin films with different heat treatment temperature. (b) The measurement result of the grain size of all the samples.

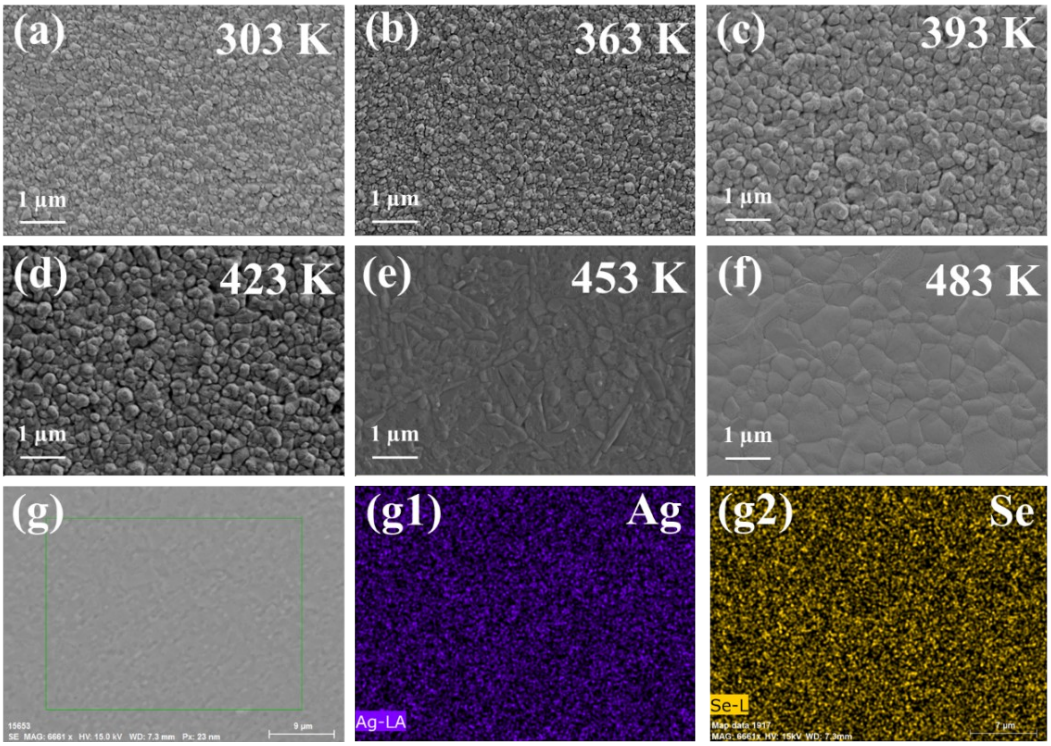

Fig. S2 SEM images of the Ag_2Se thin films at different growth temperature of (a) 303 K, (b) 363 K, (c) 393 K, (d) 423 K, (e) 453 K and (f) 483 K. (g-g2) EDS mapping for total elements and Ag/Se element of the 423 K - Ag_2Se thin film surface.

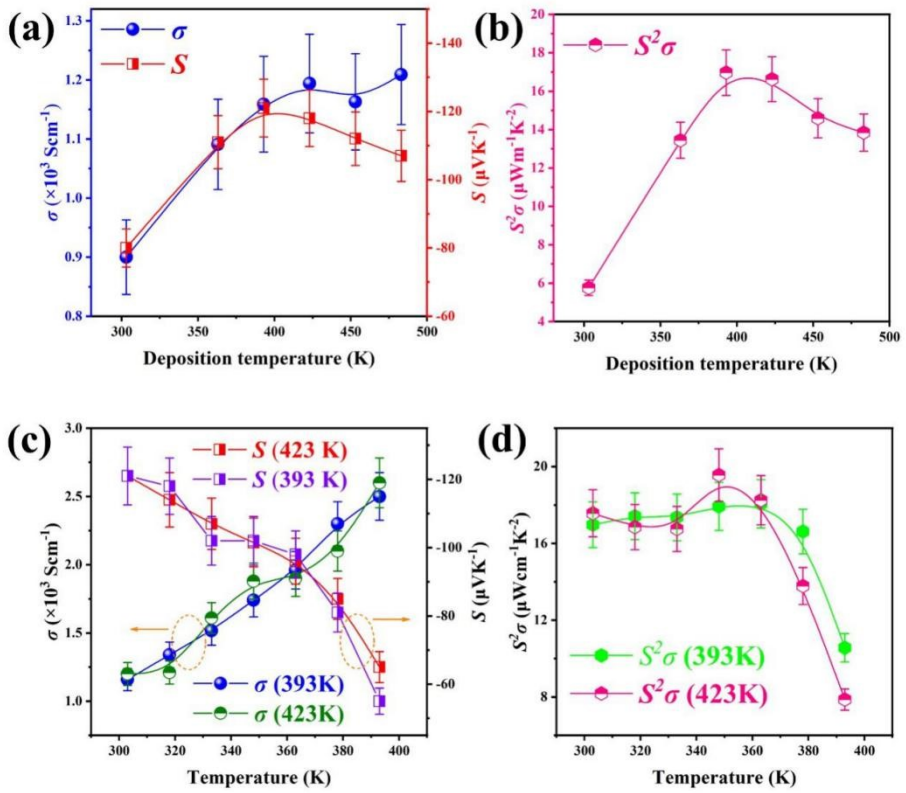

Fig. S3 (a) The deposition temperature-dependent *σ, S* and (b) $S^2\sigma$ (*PF*) of the samples at room temperature. (c) The variable test temperature-dependent *σ, S* and (d) $S^2\sigma$ (*PF*) of the samples deposited at 393 K and 423 K.

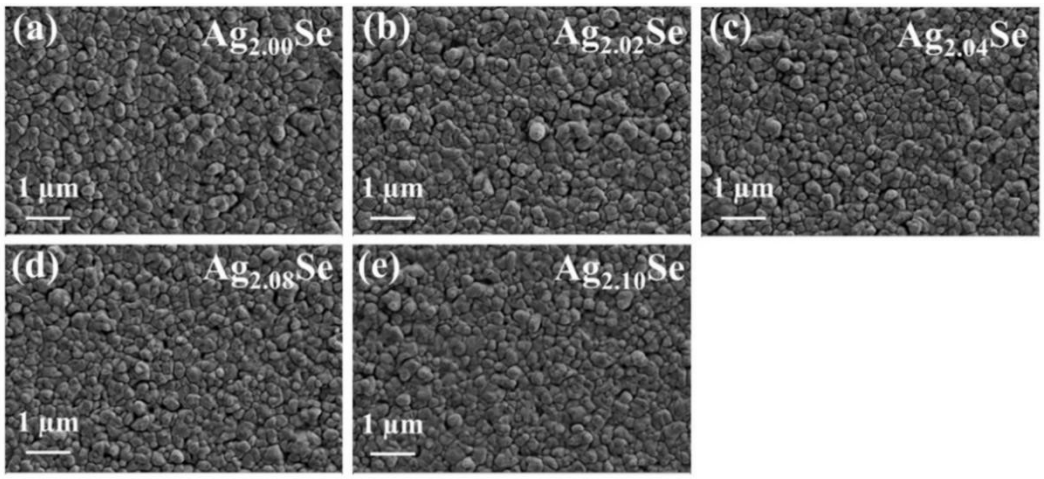

Fig. S4 SEM images of the Ag_xSe thin films at different Ag content of (a) $Ag_{2.00}Se$, (b) $Ag_{2.02}Se$, (c) $Ag_{2.04}Se$, (d) $Ag_{2.08}Se$, and (e) $Ag_{2.10}Se$.

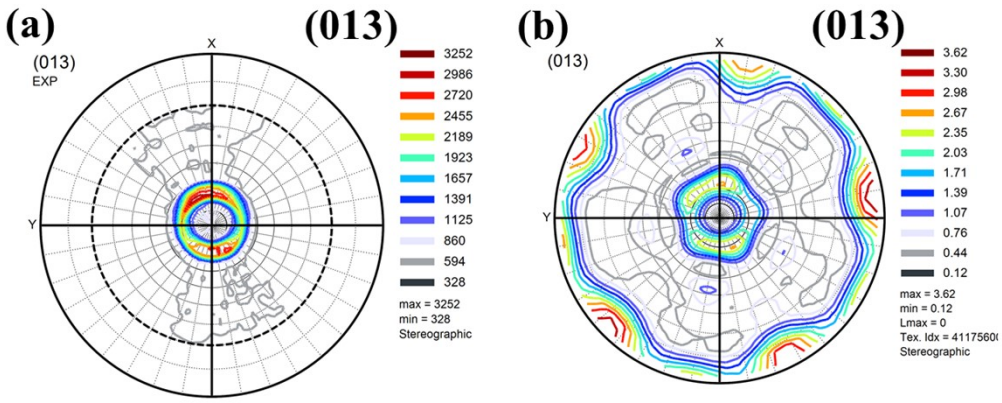

Fig. S5 (a) The (013) plane 2θ = 37.43° X-ray pole figure of $Ag_{2.02}Se$ for experiment result. (b) XRD polar figure of 2θ= 37.43° with the result after ATEX analysis (Analysis Tools for Electron and X-ray diffraction).

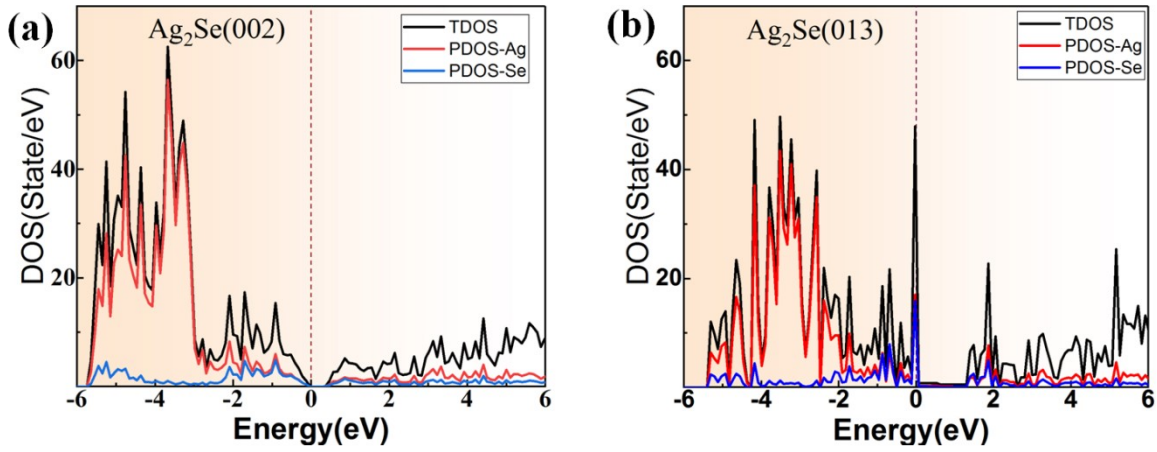

Fig. S6 Density of states of two selected crystallographic planes of (a) (002) and (b) (103).

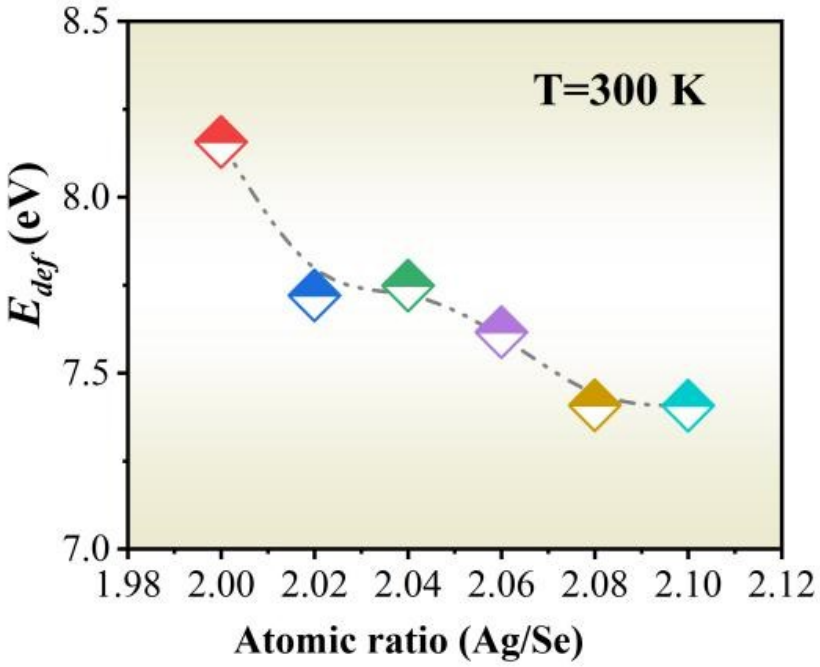

Fig. S7 The deformation potential E_{def} of Ag_2Se films with different Ag content.

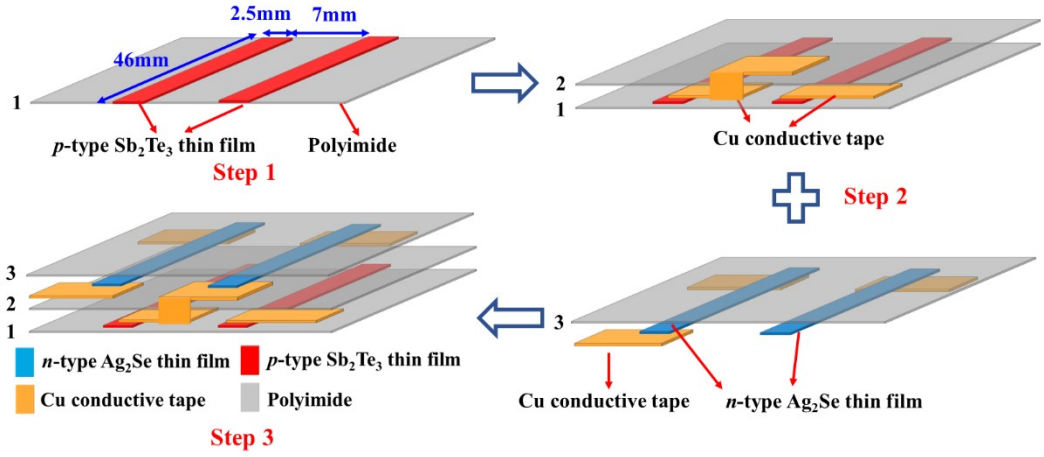

Fig. S8 Diagram of flexible device fabrication process.

It can be seen (Step 1 in Fig. S8) that the *p*-type Sb_2Te_3 legs (2.5 mm × 46 mm) with the thickness about 650 nm are prepared on polyimide substrate. The distance between each leg is about 7 mm. The copper electrode tape is pasted on the *n*-legs at one end of the polyimide substrate marked as 1 and 2. Then, *n*-type Ag_2Se thin films with the thickness about 450 nm with same size were prepared on another flexible

substrate marked as 3 as shown in step 2. Finally, *n*-type leg and *p*-type leg were connected by copper electrode tape as shown in the step 3, and the prototype flexible device was finally made by eight *p*-*n* legs.

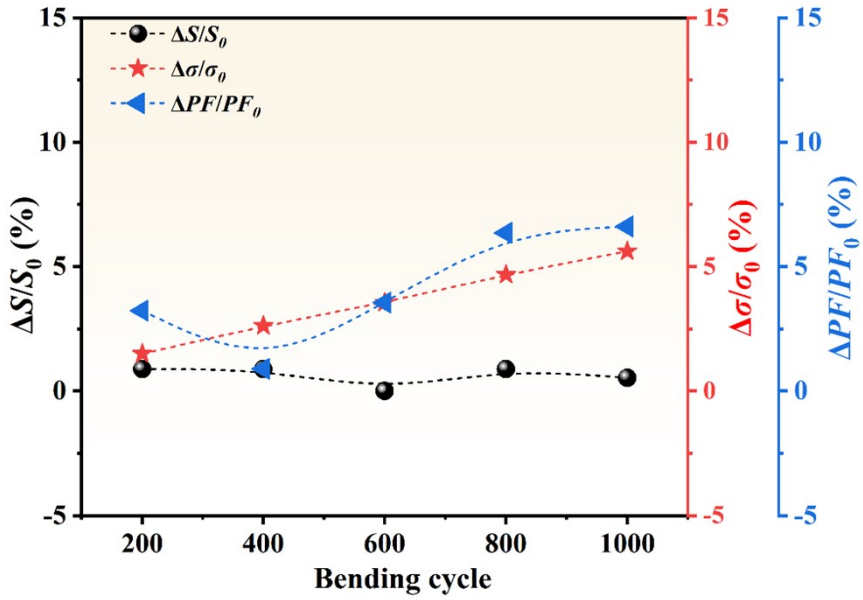

Fig. S9 The relative Seebeck coefficient change ($\triangle S/S_0$), relative electrical conductivity change ($\triangle \sigma/\sigma_0$), and relative power factor change ($\triangle PF/PF_0$) as a function of bending cycle.

Computational details:

Density functional theory (DFT) calculations were performed to investigate the electrical transport properties of Ag_2Se compound along two selected crystallographic planes of (002) and (103). The electronic properties such as the band structures and density of states (DOS) of Ag_2Se (001) and Ag_2Se (013) are achieved by using the

Vienna Ab Initio Simulation Package.[7-9] The calculations have been done by utilizing the plane-wave pseudopotential formalism. The ion-electron interaction is modeled with the help of the projector-augmented wave (PAW)[10] method for Ag and Se atoms. Cutoff energy for the wave function is set to 600 eV. The generalized gradient approximations (GGA)[11] with the Perdew-Burke-Ernzerhof potential (PBE)[12] are implemented for the exchange-correlation functional. The structures are relaxed until forces on each atom become less than 0.10^{-5} eV/Å, and the criterion for energy convergence is set as 1.0×10^{-6} eV. Both the structures are modeled by 2×2×2 supercells containing 64 Ag and 32 Se sites. A Monkhorst-Pack *k*-point mesh of 6×4×2 is used, including Γ–points for the Brillouin zone sampling of the cell in the initial self-consistent field (SCF) step and increased to 9×6×4 for the DOS calculations. The electronic energy band is plotted based on a 150 k-points grid. The equations were shown below:[13-17]

$$s(\eta) = \frac{k_B}{e} \cdot \left[\frac{\left(r + \frac{5}{2}\right) \cdot F_{r+\frac{3}{2}}(\eta)}{\left(r + \frac{3}{2}\right) \cdot F_{r+\frac{1}{2}}(\eta)} - \eta \right] \qquad (S1)$$

$$n_H = \frac{1}{e \cdot R_H} = \frac{(2m^* \cdot k_B T)^{\frac{3}{2}}}{3\pi^2 \hbar^3} \cdot \left[\frac{\left(r + \frac{3}{2}\right)^2 \cdot F_{r+\frac{1}{2}}{}^2(\eta)}{\left(2r + \frac{3}{2}\right) \cdot F_{r+\frac{1}{2}}(\eta)} \right] \qquad (S2)$$

$$\mu_H = \left[\frac{e\pi\hbar^4 \qquad C_1}{\sqrt{2}(k_B T)^{\frac{3}{2}} E_{def}{}^2 (m^*)^{\frac{5}{2}}} \right] \cdot \left[\frac{\left(r + \frac{3}{2}\right) \cdot F_{2r+\frac{1}{2}}(\eta)}{\left(r + \frac{3}{2}\right)^2 \cdot F_{r+\frac{1}{2}}(\eta)} \right] \qquad (S3)$$

$$L = \left(\frac{k_B}{e}\right)^2 \left\{ \frac{\left(r+\frac{7}{2}\right)\cdot F_{r+\frac{5}{2}}(\eta)}{\left(r+\frac{3}{2}\right)\cdot F_{r+\frac{1}{2}}(\eta)} - \left[\frac{\left(r+\frac{5}{2}\right)\cdot F_{r+\frac{3}{2}}(\eta)}{\left(r+\frac{3}{2}\right)\cdot F_{r+\frac{1}{2}}(\eta)} \right]^2 \right\} \qquad (S4)$$

where η, k_B, e, r, R_H, m^*, $\hbar$, C_1 and E_{def} are the reduced Fermi level, the Boltzmann constant, the electron charge, the carrier scattering factor (r = -1/2 for acoustic phonon scattering), the Hall coefficient, the effective mass, the reduced Plank constant, the elastic constant for longitudinal vibrations and the deformation potential coefficient, respectively. Here $C_1 = v_1^2 \cdot \rho$, where v_1 is the longitudinal sound velocity. $F_i(\eta)$ is the Fermi integral and can be expressed as:

$$F_i(\eta) = \int_0^\infty \frac{x^i}{1 + e^{(x-\eta)}} dx \qquad (S5)$$

Based on these simulations, we can plot the carrier concentration dependent m^*, and E_{def}.

Table: Magnitudes for standard values used in the calculations.

Parameter	Symbol	Magnitude
Boltzmann constant	k_B	$1.38 \times 10^{-23} J/K$
Electron charge	e	$1.6022 \times 10^{-19} C$
Reduced Plank constant	$\hbar$	$1.0546 \times 10^{-34} J.s$
Carrier scattering factor	r	$-1/2$

References

1. Y. Lu, Y. Qiu, K. -F. Cai, Y. -F. Ding, M. -D, Wan, C. Jiang, Q. Yao, C. -J. Huang,

L. -D. Chen, and J. -Q. He Ultrahigh power factor and flexible silver selenide-based composite film for thermoelectric devices. *Energy Environ. Sci.* 2020, **13**, 1240-1249.

2. C. Jiang, P. Wei, Y. -F. Ding, K. -F. Cai, L. Tong, Q. Gao, Y. Lu, W. -Y. Zhao, and S. Chen, Ultrahigh performance polyvinylpyrrolidone/Ag_2Se composite thermoelectric film for flexible energy harvesting. *Nano Energy*, 2021, **80***,* 105488.

3. Y. -T. Li, Q. Lou, J. -M. Yang, K. -F. Cai, Y. Liu, Y. -M. Lu, Y. Qiu, Y. Lu, Z. -X. Wang, M. -M. Wu, J. -Q. He, and S. Shen, Exceptionally High Power Factor Ag_2Se/Se/Polypyrrole Composite Films for Flexible Thermoelectric Generators. *Adv. Funct. Mater.* , 2022, **32***,* 2106902.

4. Y. Lu, Y. -F. Ding, Y. Qiu, K. Cai, Q. Yao, H. -J. Song, L. Tang, J. -Q. He, L. -D. Chen, Good Performance and Flexible PEDOT:PSS/Cu_2Se Nanowire Thermoelectric Composite Films, *ACS Appl. Electron. Mater.* **2019**, 11, 12819-12829.

5. L. Wang, Q. Yao, W. Shi, S. Qu, and L. Chen, Engineering Carrier Scattering at the Interfaces in Polyaniline Based Nanocomposites for High Thermoelectric Performances. *Mater. Chem. Front.*, 2017, **1***,* 741-748.

6. Shang, H. et al. $Bi_{0.5}Sb_{1.5}Te_3$-Based Films for Flexible Thermoelectric Devices. *J. Mater. Chem. A*, 2020, **8***,* 4552-4561.

7. G. Kresse, and J. Furthmuller, Efficiency of ab-initio total energy calculations for metals and semiconductors using a plane-wave basis set, *Comp. Mater. Sci.*, 1996, **6**, 15-50.

8. G. Kresse, and J. Furthmuller, Efficient iterative schemes for ab initio total-energy calculations using a plane-wave basis set, *Physical Review B*, 1996, **54**, 11169-11186.

9. G. Kresse, Hafner, and J. Hafner, Ab initio molecular-dynamics for liquid-metals,

Phys. Rev. B, 1993, **47**, 558-561.

10. G. Kresse, and D. Joubert, From ultrasoft pseudopotentials to the projector augmented-wave method, *Phys. Rev. B*, 1999, **59**, 1758-1775.

11. J. -P. Perdew, K. Burke, and M. Ernzerhof, Generalized Gradient Approximation Made Simple, *Phys. Rev. Lett.*, 1996, **77**, 3865.

12. J. -P. Perdew, K. Burke, and M. Ernzerhof, Erratum: generalized gradient approximation made simple, *Phys. Rev. Lett.*, 1997, **78**, 1396-1396.

13. Y. Xu, W. Li, C. Wang, J. Li, Z. Chen, S. Lin, Y. Chen and Y. Pei, Performance optimization and single parabolic band behavior of thermoelectric MnTe, *J. Mater. Chem. A*, 2017, **5**, 19143-19150.

14. J. Shen, Z. Chen, S. lin, L. Zheng, W. Li and Y. Pei, Single parabolic band behavior of thermoelectric p-type $CuGaTe_2$, *J. Mater. Chem. C*, 2016, **4**, 209-214.

15. X. She, X. Su, H. Du, T. Liang, G. Zheng, Y. Yan, R. Akram, C. Uher and X. Tang, High thermoelectric performance of higher manganese silicides prepared by ultra-fast thermal explosion, *J. Mater. Chem. C*, 2015, **3**, 12116-12122.

16. W. Liu, X. Shi, M. Hong, L. Yang, R. Moshwan, Z. G. Chen and J. Zou, *J. Mater. Chem. C*, 2018, **6**, 13225.

17. S. Y. Wang, X. Y. She, G. Zheng, F. Fu, H. Li, and X. F. Tang, Enhanced Thermoelectric Performance and Thermal Stability in β-Zn_4Sb_3 by Slight Pb-Doping, *Journal of Electronic Materials*, 2012, **41**, 1091-1099.